ASME Journal of Manufacturing Science and Engineering
Online journal at:
https://asmedigitalcollection.asme.org/manufacturingscience

The Microstructural Origins of Acoustic Emission Signatures Encountered During Fracture Cutting of Bovine Cortical Bone

Roshan Mishra[1]
Department of Mechanical Aerospace and Nuclear Engineering,
Rensselaer Polytechnic Institute,
110 8th Street,
Troy, NY 12180
e-mail: mishrr2@rpi.edu

Michael Conward[2]
Department of Mechanical Aerospace and Nuclear Engineering,
Rensselaer Polytechnic Institute,
110 8th Street,
Troy, NY 12180
e-mail: conwam5@rpi.edu

Johnson Samuel[3]
Associate Professor
Department of Mechanical Aerospace and Nuclear Engineering,
Rensselaer Polytechnic Institute,
110 8th Street,
Troy, NY 12180
e-mail: samuej2@rpi.edu

This paper is aimed at studying the acoustic emission signatures of dominant failure mechanisms encountered during fracture cutting of bovine cortical bone. This is achieved through an orthogonal cutting study performed in a sensor-rich environment comprising a cutting force sensor, acoustic emission sensor, and a high-speed camera. The synchronization of these three sensing modalities allows for the visual identification of the dominant failure modes, while also mapping them to their corresponding acoustic and cutting force metrics. Given their distinctly different underlying microstructures, the haversian and plexiform components of the bovine cortical bone are investigated separately. A total of six dominant failure mechanisms have been confirmed across the haversian and plexiform bone types. Osteon fracture and trans-lamellar fracture have been identified as the mechanisms expending the maximum energy during the fracture cutting of haversian and plexiform bone, respectively. Overall, the acoustic emission and the cutting force metrics are seen to be complementary in characterizing the six failure mechanisms. The findings of this work have implications for tool-mounted sensing modalities that could be used to detect "in-process" failure mechanisms during bone surgical procedures.
[DOI: 10.1115/1.4062728]

Keywords: bovine cortical bone, acoustic emission, fracture cutting, failure mechanisms, biomedical manufacturing, machining processes

1 Introduction

Despite the widespread success of routine bone surgical procedures, clinical studies have shown that about ~20% of the patients remain unsatisfied with their surgery outcomes [1–5]. For total joint replacement surgeries of the knee and the hip, this implies that the patients would have to undergo revision surgeries, due to reasons such as fractures, infection, and instability of the bone–metal interface, all of which can be traced back to the damage inflicted on the bone surface during the surgery [1–5]. As such, the in-process monitoring, characterization, and subsequent minimization of specific damage mechanisms are all critical to the success of bone surgical procedures.

Orthogonal bovine cortical bone-cutting studies have been used, since the 1970s, to investigate damage mechanisms relevant to bone surgical procedures [6–14]. Bovine cortical bone can be cut in either a predominantly shear-dominated or a fracture-dominated mode [9]. The literature points to a depth-of-cut value $\geq \sim 60\ \mu$m being the transition threshold to move from a predominantly shear-dominated to a fracture-dominated mode of cutting. Most of the bone-cutting studies in the literature have focused primarily on the shear-cutting mode [6–11] with few fundamental investigations into fracture-dominated regimes of cutting [12–15]. Furthermore, these studies have only explored the use of workpiece/tool-mounted load cells as the in-process sensing modality of interest. Acoustic emission (AE) sensors have been known to be sensitive to progressive damage in composite materials [16–18]; however, their use in bone-cutting studies has been limited to gross tool-path planning applications such as detection of the boundary between cortical and cancellous bone [19,20] and more recently in shear-dominated bone-sawing studies [21].

Given the current state of the literature, this paper is aimed at studying the microstructural origins of the acoustic emission signatures encountered during fracture cutting of bovine cortical bone. The failure modes encountered during orthogonal cutting are identified through the synchronization of a high-speed camera with a tool-mounted cutting force and acoustic emission sensor. Six distinct failure mechanisms are identified spanning the haversian and plexiform regions. The acoustic energy per unit crack area and the cutting force per unit crack area are used as complementary metrics to distinguish the failure mechanisms.

The remainder of this paper is organized as follows. Section 2 provides an overview of the microstructure of the bovine cortical bone. It also discusses the details of the sensor-rich testbed and associated protocols used for this fracture-cutting study. Section 3 discusses the experimental findings including the six major failure mechanisms and their

[1]Currently at Intel Corporation, OR.
[2]Currenty at SelfArray, NY.
[3]Corresponding author.
Manuscript received February 5, 2023; final manuscript received June 3, 2023; published online July 13, 2023. Assoc. Editor: Robert Chang.

dominant acoustic energy and cutting force metrics. These findings are benchmarked against existing AE literature. Finally, Sec. 4 presents the specific conclusions that can be drawn from this work.

2 Materials and Methods

2.1 Microstructure Characterization. Bovine cortical bone samples of 10 mm length × 10 mm width were harvested from a ~30-month-old cow using a Mar-med™ bone saw under constant water irrigation. These samples were then polished down to an average thickness of ~500 μm to eventually obtain four specimens of haversian bone and eight specimens of plexiform bone. Additional details about the protocols used for sample extraction, storage, and handling can be found in Refs. [10,11].

Care was taken to ensure a hydrated state for the bone samples both for microstructure characterization as well as the cutting studies. The samples for microstructure characterization were polished using 5 μm and 1 μm alumina slurry on a wet polishing pad and then imaged after staining with a toluidine blue dye [10,11]. Imaging was performed on the samples using a conventional optical microscope. The contrast provided by the blue dye did not necessitate a need for decalcification of the bone samples. Figures 1(*a*) and 1(*b*) show the typical microstructure seen in the haversian and plexiform regions. While a detailed discussion of the microstructural features and their nanoindentation characterization is also provided in Refs. [11,12], a brief review of the key microstructural characteristics is provided here for purposes of continuity.

As shown in Fig. 1, the bovine cortical bone consists of haversian and plexiform regions that are easily distinguishable by their underlying microstructure. Haversian bone comprises cylindrical osteons embedded in an interstitial matrix [10,11]. Osteons consist of concentric lamellae surrounding haversian canals. The interface between the osteons and the interstitial matrix is characterized by the presence of a cement line.

Bovine cortical bone is anisotropic in nature with directionally varying mechanical properties and fracture behaviors that are influenced by the hydration state of the sample [8,22–24]. The prior work of Conward and Samuel [10–12] report the nanoindentation-based characterization of the microstructures identified in the plane-of-view of Fig. 1. In terms of mechanical properties, the interstitial matrix has slightly higher elastic modulus and hardness than the osteons, while the cement line has lower modulus and hardness than both the osteon and the interstitial matrix [10–12]. Plexiform bone consists of alternating layers of woven and lamellar regions, giving it an appearance of a sandwich-structured composite [10–12]. The lamellar regions also contain blood vessels inside them. Table 1 denotes the average values of the key microstructural features present in the bovine cortical bones used in this study. The

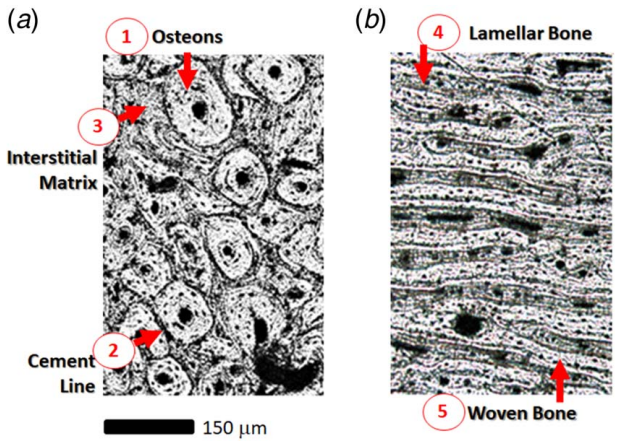

Fig. 1 Bone microstructure (*a*) haversian and (*b*) plexiform (scale = 150 μm)

Table 1 Size range for key microstructural attributes [25]

Haversian bone	
Osteon diameters	140–190 μm
Cement-line thickness	10–18 μm
Haversian canal diameter	30–40 μm
Osteon length	3–5 mm
Plexiform bone	
Lamellar bone length	150–1200 μm
Lamellar bone thickness	35–65 μm
Woven bone length	350–1120 μm
Woven bone thickness	50–90 μm

Note: The values were measured from 10 micrographs of the two bone types. Relative hardness and Young's modulus values can be found in Ref. [11].

woven bone has superior mechanical properties to the lamellar bone as reported in Refs. [11,12].

2.2 Orthogonal Fracture Cutting Experiments. The cutting experiments in this study were designed to induce fracture-dominated failure in the distinct microstructural components of bovine cortical bone. Figure 2 outlines the overall experimental setup, which is similar to the one used by Conward and Samuel [10,12] for orthogonal shear cutting of bovine cortical bone. The experiments were conducted on a three-axis micro-machining center (Mikrotools™ DT-110, Singapore) using a precision-ground, tungsten carbide, single-point cutting tool. The cutting tool had a rake angle of (+20 deg) and a clearance angle of 1 deg. The 7 mm width of the straight cutting edge was designed to be considerably higher than the thickness of the sample (~500 μm). The larger tool width ensured that orthogonal cutting conditions were met while also making it convenient to perform multiple cutting experiments without the concern of tool wear.

The bone samples (10 mm length × 10 mm width) were mounted on an aluminum carrier plate attached to the *X*–*Z* plane of the micro-machining platform (Fig. 2(*b*)). The workpiece was imparted a linear cutting velocity of 800 mm/min while the tool was held stationary (Fig. 2). While this cutting velocity value was chosen based on prior bone cutting studies [6,26,27] and the linear-speed limitations of the micro-machining platform [10,12], the results presented here should be interpreted with caution for surgical procedures such as bone sawing, where the cutting speeds could be as high as 3–4 m/s [10]. The depth-of-cut was maintained at 70 microns to ensure fracture-dominated cutting of bovine cortical bone [9,12–15]. This depth-of-cut value was chosen based on the results of our preliminary experiments [12,28] as well as the findings from literature associated with fracture cutting of bovine cortical bone [9,12–15]. It should be noted that the depth-of-cut is ~50% of the osteon diameters and is at least equal to or greater than the thickness of the lamellar/woven bone (refer to Table 1).

The sensing modalities implemented for this study include the use of (i) Kistler 9256C1 dynamometer to measure the cutting forces; (ii) Nano-30 AE sensor (Physical Acoustics Inc., response frequency 150–750 KHz) to detect the acoustic emission generated during fracture cutting; and (iii) a Phantom V.7.3 high-speed camera and a Prior Lumen light-source to observe the fracture cutting process. As shown in Fig. 2(*b*), the cutting tool-post was mounted directly onto the Kistler dynamometer. The acoustic emission sensor was attached to the shank of the tool using vacuum grease as a coupling agent and a magnetic pre-load mounting arrangement similar to that reported in the bone sawing experiment by Mishra et al. [21]. The high-speed camera and associated optics were positioned to focus on the stationary tool cutting-edge during the cutting process. It should be noted that this configuration of the sensor-suite ensured that specific failure modes encountered in the cutting zone were now "observable" to the sensors, thereby resulting in two benefits. First, the underlying microstructure of the

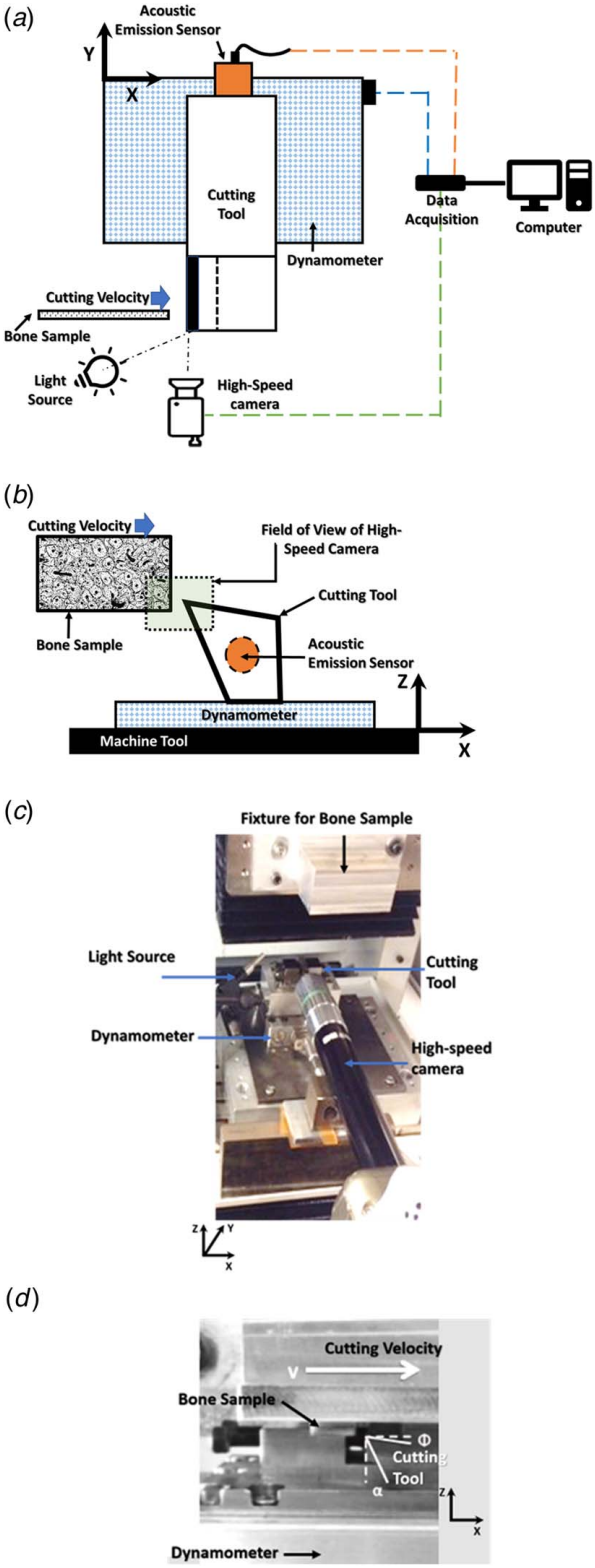

Fig. 2 Orthogonal cutting experiment setup: (*a–b*) Not to scale cartoon of the top view, and front view, (*c*) sample retracted view of the experimental setup, and (*d*) closeup of the cutting tool with respect to the bone sample

sample and its associated failure mode could be visually identified in the high-speed images. Second, more critically this meant that the corresponding temporal cutting force and acoustic emission signals could then be subsequently "tagged" for specific failure mechanisms of interest.

Table 2 Orthogonal fracture cutting conditions

Workpiece	• Haversian bone • (Plexiform—0 deg): Plexiform bone cut at 0 deg to lamellar bone • (Plexiform—90 deg): Plexiform bone cut at 90 deg to lamellar bone • Age of Cow: ~30 months • Average specimen thickness : ~500 μm • Length of cut ~10 mm
Tool	• High-precision-ground tungsten carbide, 1 μm edge radius, 10-deg clearance angle, +20-deg rake angle
Cutting velocity	• 800 mm/min
Depth of cut	• 70 μm

The orthogonal fracture cutting experiments were conducted on different haversian and plexiform bone specimens. Plexiform bone specimens were cut in two directions, namely, 0 deg and 90 deg to the woven/lamellar orientation as these orientations are expected to result in different failure modes. These orientations will be denoted as Plexiform-0 deg and Plexiform-90 deg, respectively, for the remainder of this paper. For each Haversian, Plexiform-0-deg and Plexiform-90-deg samples, four replicate cutting experiments were conducted. A National Instruments data acquisition system was used to collect the cutting force signals at a sampling rate of 30 KHz and acoustic signal at a sampling rate of 4 MHz. The high-speed camera images were collected at 4000 frames per second. Matlab was used for all subsequent data analysis. Table 2 shows the cutting conditions used in this study.

The anisotropy in the mechanical properties of the bovine cortical bone [22–24] also translates to differences in the cutting responses seen at varying cutting-edge orientations with respect to the osteonal axis [8]. It should be noted that the orthogonal cutting experiments presented in this paper are in the "across" direction as identified in Ref. [10]. The transverse/perpendicular and longitudinal/parallel directions [8] represent more complex modes of fracture and remain an open area of investigation.

3 Results and Discussion

This section presents the experimental findings from the orthogonal cutting studies. First, an overview of the major fracture events observed in the samples is presented. The high-speed images are then used to correlate specific failure mechanisms seems within the Haversian, Plexiform—0 deg, and Plexiform—90 deg samples with their characteristic acoustic emission signatures. Following this, a discussion on the quantitative analysis of the acoustic emission and cutting force signals is presented.

3.1 Overview of Dominant Failure Mechanisms. As described in Sec. 2, fracture cutting was performed at a depth-of-cut of 70 μm for the Haversian, Plexiform—0 deg, and Plexiform—90 deg samples, respectively. With four replicates being done for each of the three samples, the experimental matrix allowed for the observation of dominant failure modes. Figure 3 outlines these dominant fracture events. It should be noted that for a given cutting tool configuration, these specific failure modes and the metrics associated with their acoustic signatures are a function of (i) the original microstructural variation within the volume of the cut; and (ii) the orientation of the microstructural constructs with respect to the cutting velocity.

Figure 3(*a*) depicts three key failure mechanisms seen in the haversian sample, namely, (i) *cement-line fracture* (or *osteon debonding);* (ii) *osteon fracture*; and (iii) *interstitial matrix fracture*. In *cement-line fracture*, the crack is primarily seen to result in

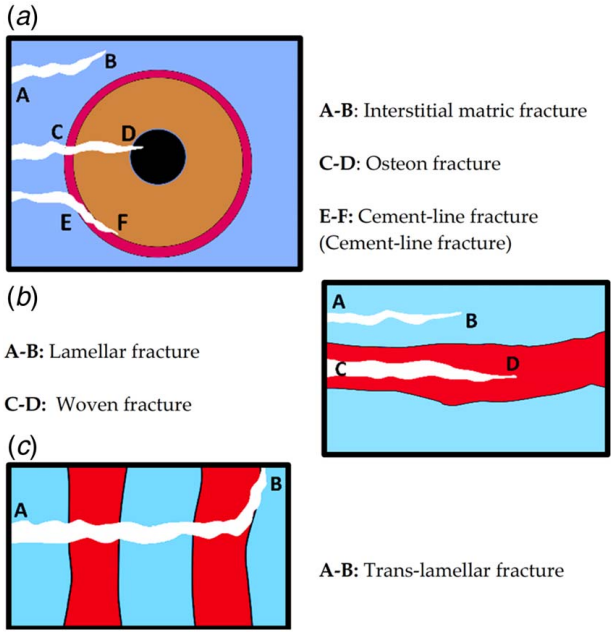

Fig. 3 Cartoons of specific failure mechanisms observed during fracture cutting of bovine cortical bone (Note: (*a*) Haversian bone is shown as osteons embedded in interstitial matrix; and (*b*–c) plexiform bone is shown as alternating layers of lamellar and woven regions)

failure along the cement line, as shown using crack path *E–F* in Fig. 3(*a*). *Osteon fracture* involves the crack passing through the osteon as it cuts through the concentric lamella. This is shown using crack path *C–D* in Fig. 3(*a*). The *interstitial matrix fracture* indicates a distinct fracture event that is limited to the interstitial matrix and is denoted by crack path *A–B* in Fig. 3(*a*).

For the plexiform bone, the specific failure mechanisms are a function of the orientation of the lamellar structures with respect to the cutting velocity. In the Plexiform—0-deg case, where the cutting velocity is parallel to the orientation of the lamellar/woven structures, the dominant failure mechanisms include (i) *lamellar fracture* and (ii) *woven fracture*. As shown in Fig. 3(*b*), in these cases, the cracks initiate, propagate, and terminate within the two distinct phases, with crack paths *A–B* and *B–C* depicting *lamellar fracture* and *woven fracture*, respectively. While a crack crossover between the lamellar and woven regions is possible based on the relative location of these regions with respect to tool path, the relative thickness of the woven/lamellar regions (refer to Table 1) compared to the 70 μm depth of cut ensured that such crossover events were not dominant in the Plexiform—0-deg case.

For the Plexiform—90-deg case, the cutting velocity is perpendicular to the orientation of the lamellar/woven structure. As shown in Fig. 3(*c*) *trans-lamellar fracture* is the dominant mode of failure in this case where the crack path *A–B* is seen to cut through multiple woven/lamellar structures. This pattern of failure is similar to that seen in unidirectional carbon fiber composites when the cutting velocity is perpendicular to the orientation of the fibers [29]. It should be noted that all major fracture events described here, except for trans-lamellar fracture were first observed by Conward [28] during investigations into fracture cutting of age-varying bovine cortical bone.

3.2 Representative Cutting Force and Acoustic Emission Signals. The cutting force and acoustic emission signals provide complementary information regarding the failure process encountered during fracture cutting of bovine cortical bone. Figures 4(*a*) and 4(*b*) show a representative correlation between the cutting force and the acoustic emission signal obtained during a 100-ms long cut involving the haversian bone. Figures 4(*c*) and 4(*d*) show a closeup of the circled region in Figs. 4(*a*) and 4(*b*). As seen in these images, the cutting force signals are characterized by distinct peaks and valleys that have a direct correlation to specific AE bursts. Unlike the continuous AE signal obtained during the shear-dominated bone sawing process [21], here the AE events are observed to be a discrete series of bursts. The data from the high-speed images (discussed ahead in Secs. 3.3–3.5) confirm that the AE bursts correspond to the occurrence of distinct underlying "crack-opening" events corresponding to cutting force drops. The bursts have different peak amplitudes, indicating that the underlying energy expended in each of these distinct fracture events is different. Overall, the peak magnitude of the AE bursts has little correlation to the corresponding magnitude of the cutting force. This also implies that the AE signal is clearly generated during crack-opening events and is likely influenced by the resistance faced by the crack path. Sections 3.3 and 3.4 ahead deal with the use of temporally correlated images from the high-speed camera to visually identify the bursts corresponding to the distinct failure mechanisms. Section 3.5 deals with the analysis of the cutting force and AE signals to extract distinguishing features underlying the specific failure mechanisms.

3.3 Failure Mechanisms in Haversian Bone. Given the relatively large percentage area occupied by the osteons, *cement-line fracture* and *osteon fracture* were the major mechanisms observed in the haversian bone sample with *interstitial matrix fracture* being observed in some select regions within the cutting volume. Figure 5(*a*) shows a representative high-speed imaging frame corresponding to *cement-line fracture* and its corresponding AE signature burst. As can be seen, in this failure mode, the crack is initiated at the tool tip and propagates clearly along the cement line resulting in the complete removal of the underlying osteon. The corresponding AE burst is characterized by a single burst with a relatively low peak amplitude of ~0.1 V.

Figure 5(*b*) depicts the high-speed images and AE signal corresponding to a characteristic *osteon fracture* event. In general, this failure mode was observed to have 2–3 AE bursts corresponding

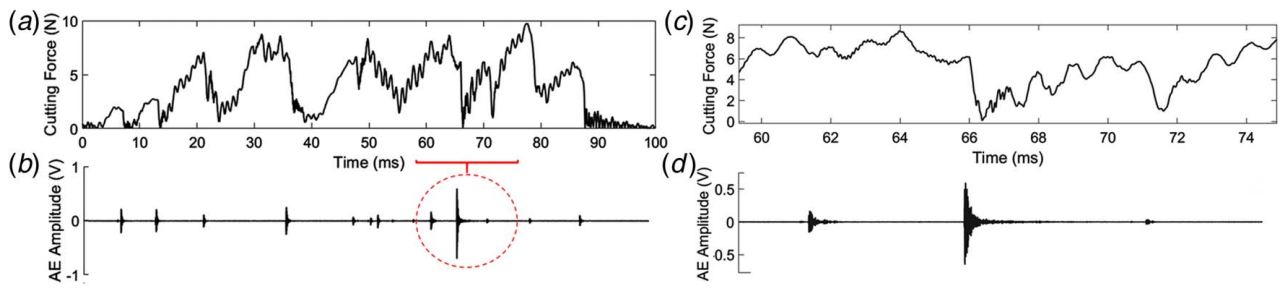

Fig. 4 Representative cutting force and acoustic emission signals for haversian bone: (*a*) cutting force signal 100 ms duration, (*b*) AE signal 100 ms duration, and (c–*d*) cutting force and AE signal overlay for the circled region in (*a–b*)

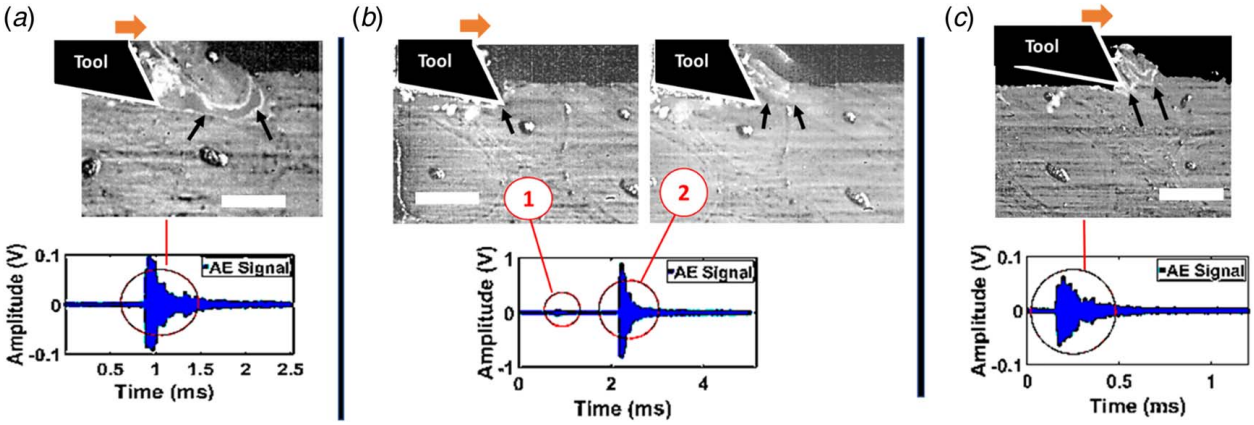

Fig. 5 Acoustic emission signatures of specific failure mechanisms observed during fracture cutting of haversian bone: (*a*) cement-line fracture (i.e., osteon debonding), (*b*) osteon fracture, and (c) interstitial matrix fracture (scale bar on high-speed images = 150 μm).

to distinct stages of the *osteon fracture*. As seen in Fig. 5(*b*), first the crack is initiated by the tooltip in the outer circumferential lamellae of the osteon resulting in a small initiating AE burst signal. After this, the crack propagates through the lamellae, thereby removing a major portion of the osteon. The crack propagation through the concentric lamellae is an energy-intensive process [16] as indicated by the higher magnitude of the following AE burst (refer to Fig. 5(*b*)). At times depending on the orientation of the osteon and the relative size of the haversian canal, there are multiple AE bursts that correspond to crack propagation from (i) the outer circumferential lamellae toward the haversian canal; (ii) the haversian canal to the outer circumferential lamellae.

Figure 5(*c*) depicts the high-speed images and AE signal corresponding to a characteristic *interstitial matrix fracture* event. The isotropic nature of the interstitial matrix is likely responsible for this fracture event resulting in a predominantly single burst.

3.4 Failure Mechanisms in Plexiform Bone. The plexiform bone comprises alternate layers of woven and lamellar bone. The

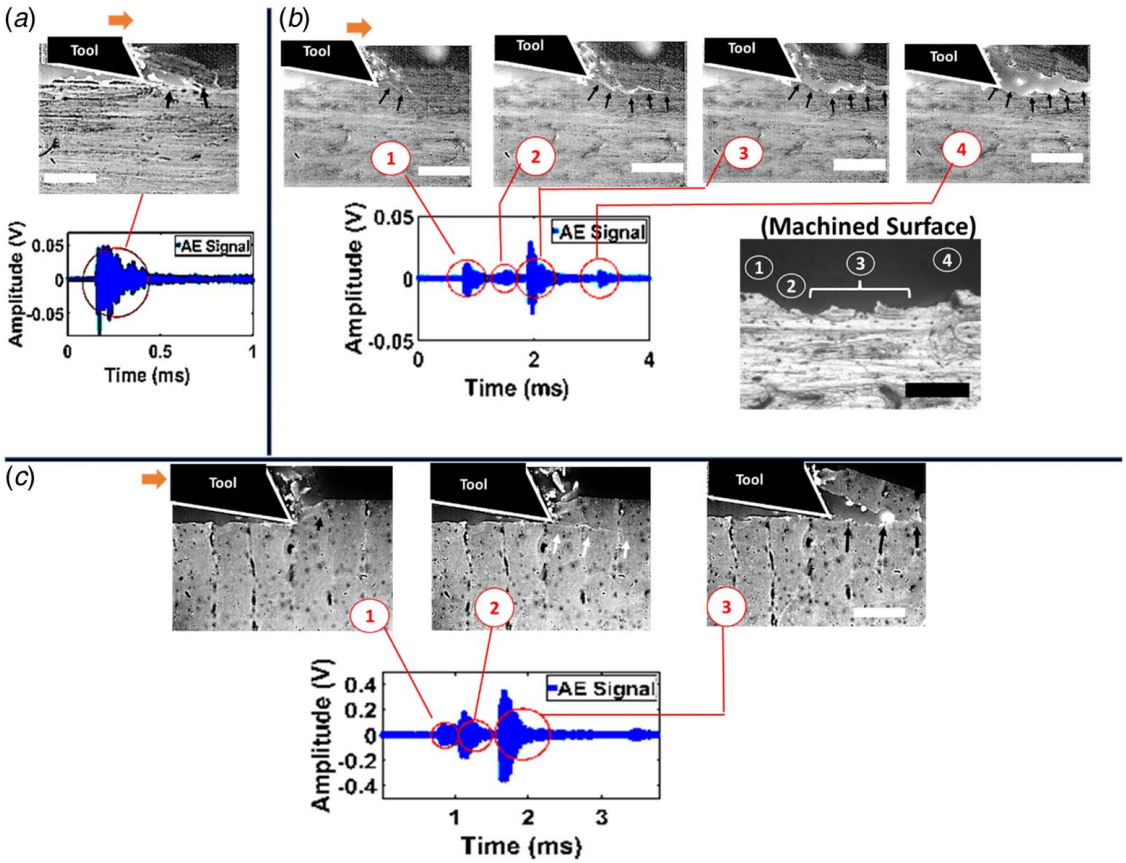

Fig. 6 Acoustic emission signatures of specific failure mechanisms observed during fracture cutting of plexiform bone: (*a*) woven fracture (Plexiform—0-deg orientation), (*b*) Lamellar fracture (Plexiform—0-degorientation), and (*c*) Trans-lamellar fracture (Plexiform—90-deg orientation (scale bar on high-speed images = 150 μm))

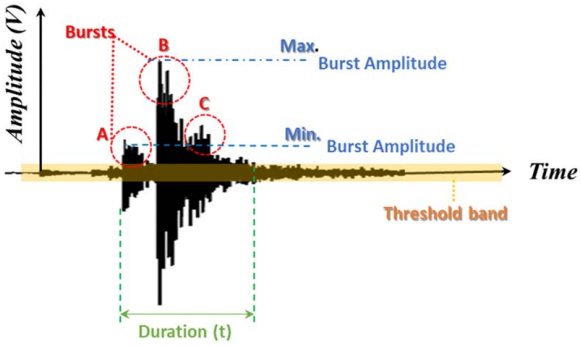

Fig. 7 Key calculated metrics associated with acoustic emission signals

woven bone has a higher Young's modulus/hardness and is also isotropic in nature when compared to the softer lamellar bone [28].

3.4.1 Plexiform—0-Deg Orientation. As shown in Fig. 6(*a*), *woven fracture* in the plexiform—0-deg case results predominantly in a single burst event with no clear distinguishing features. This is in stark contrast to the *lamellar fracture* event shown in Fig. 6(*b*) where the crack is seen to be initiated by the tooltip in the outer lamellae resulting in an AE burst (denoted as burst No.1). After this, the crack is seen to propagate progressively in the lamellar region ahead of the tool resulting in periodic bursts in the AE signal (Fig. 6(*b*), burst Nos. 2–4. The correlation between the high-speed images and the resulting machined surface (Fig. 6(*b*)) implies that these bursts correspond to distinct redirections of the crack based on the anisotropic properties encountered within the lamellar bone. Typically, this failure mechanism is observed to end with a bending-related chip breakage seen while cutting carbon fibers in a similar orientation [29].

3.4.2 Plexiform—90-Deg Orientation. As seen in Fig. 6(*c*), this orientation results in a *trans-lamellar fracture* where the crack originates in one of the phases and propagates through multiple lamellar/woven structures before the removal of the chip. The AE signature reveals multiple bursts that correspond to crack initiation, propagation, and eventual chip removal. The bursts corresponding to the crack propagation are seen to correlate to the number of woven–lamellar interfaces crossed by the crack.

3.5 Distinguishing Features of the Acoustic Emission Signals. After imposing a threshold of 1.5 mV to account for noise, the start and end of the AE signals were first identified. Then, the synchronized high-speed images were used to isolate the failure mechanism-specific AE signals. Figure 7 shows a typical AE signal along with the key metrics extracted for the purposes of visual distinction between the failure modes. These include the following:

- *Number of Bursts*: The number of bursts corresponds to the number of distinctly separate amplitude regions seen in the AE signature corresponding to the failure mechanism. For the signal indicated in Fig. 7, there exist three bursts labeled A, B, and C in Fig. 7.
- *Ratio of Maximum/Minimum Burst Amplitude*: This ratio corresponds to the maximum and minimum amplitude seen within the bursts associated with the failure mechanism. The two extreme amplitudes are indicated in Fig. 7.

Table 3 summarizes the differentiating metrics across all six failure mechanisms. In the haversian case, *osteon fracture* resulted in the highest number of bursts as well as the maximum value of the amplitude ratios. For the plexiform case, the *trans-lamellar fracture* resulted in the maximum amplitude.

In addition to the aforementioned visually distinguishing features present in the AE signal, the acoustic energy per unit crack area (i.e., normalized AE energy denoted as W_{AE}) was also calculated. This is given by the expression

$$W_{AE} = \frac{\sum_{i=1}^{n} x_i^2}{t * \int_C ds}$$

where n is the number of samples (data points) in the AE signal corresponding to a specific failure mechanism, x_i is the amplitude of ith data sample, t is the thickness of the sample, and $\int_C ds$ is the line integral of the crack length. It should be noted that the denominator of this expression is an estimate of the resulting crack area with the thickness t being measured specifically for each sample before the experiments. The overall crack length specific for a failure mechanism was obtained by using a combination of the high-speed images and the associated observations of the machined surface morphology (refer to Fig. 6(*b*)). The protocols for crack length estimation followed here are based on those laid out in Refs. [12,28]. In addition, the average cutting force data specific to each of the failure mechanisms were used to calculate a comparable cutting force per unit crack area metric.

Figures 8(*a*) and 8(*b*) show the normalized acoustic energies (W_{AE}) and the cutting force per unit crack area values, respectively, for each of the specific failure mechanisms. It should be noted that the acoustic energies are plotted on a log scale given the orders of magnitude difference that exists for the range of values seen for different failure mechanisms. In general, the two plots appear to be well correlated for each of the failure mechanisms. For the haversian bone, osteon debonding due to *cement-line fracture* consumes the lowest energy during fracture cutting. This is backed up by the fact that within the haversian bone type, the range of values seen for both these metrics is the lowest for this failure mechanism. This trend can be attributed to the lower hardness of the cement line in comparison to the osteon and the interstitial matrix [11]. The *osteon fracture* is seen to offer the most resistance to crack propagation. This could be explained by the resistance to fracture provided by the presence of concentric lamella in the osteons in haversian bone [16].

For the plexiform bone, the *trans-lamellar fracture* observed while cutting at 90 deg to the orientation of the lamella is seen to offer the most resistance to crack propagation. This is in line with the observations made in conventional composites where the reinforcing fibers are oriented at 90 deg to the cutting velocity [29]. While the range of AE values seen for the lamellar and woven fracture in the Plexiform—0 deg case are comparable, the cutting force data reveals that the lamellar fracture requires the lower cutting force per unit crack area.

The data show that the AE energies are clearly able to identify the lowest energy-consuming failure mode for the haversian case and the highest energy-consuming mode for the plexiform case. However, for the other cases, there is an overlap in the range of AE values, even though statistical differences exist between the corresponding force magnitudes seen in Fig. 8(*b*). In such cases, the complementary data revealed by both these signals could be used to estimate a clearer picture of the failure mechanics.

In general, the dominant frequency range of all AE signals lay in the range of 265–300 KHz. However, only time-domain analysis of the AE signals has been discussed in this paper since the spectrograms associated with the AE signals did not reveal any distinguishing frequency bands corresponding to underlying failure mechanisms. This is attributed to the fact that the AE sensor was mounted to the tool and not to the bone sample. This framework of sensor attachment is unlike other material testing/characterization applications where the AE sensor/s are directly attached to the material of interest [16,30–32]. In those cases, the frequency bands present in the AE signal can distinguish the influence of key microstructure components. In contrast, here the AE sensor essentially measures the elastic waves generated in the cutting tool. As such

Table 3 Differentiating acoustic emission signatures

Haversian bone	Cement-line fracture	Osteon fracture	Interstitial matrix fracture
No. of AE "bursts"	1	2–3	1 (at times) > 1 *
Max/min amplitude ratio	1	10–24	
Plexiform bone	**Woven fracture (Plexiform—0-deg)**	**Lamellar fracture (Plexiform—0 deg)**	**Trans-lamellar fracture (Plexiform—90-deg)**
No. of AE bursts	1 (at times) > 1 *	≥4	≥3
Max/min amplitude ratio		1–6	5–8

*Indicates a value ≥ 1; however, differentiating range could not be established given the wide variation in the experimental data due to the isotropic nature of the phase [10,28].

the only distinguishing characteristic of the AE signal is the amplitude and energy of the "AE event".

3.6 Comparisons With Existing State of Literature. Acoustic emission-based monitoring of bone has been studied in the literature under the distinct categories of material testing/characterization [16,30–32] and cutting [19–21]. In the material testing/characterization literature, the AE sensor is always attached to the bone sample being tested and distinct failure events are characterized using characteristic AE frequency ranges [16,30–32]. These macro-scale experiments involve testing the femur under conventional modes of bending, torsion, tension, and compression. As such, this category of literature is primarily related to the identification of fracture onset in the femur, as indicated by the frequency bands present in the AE signal [16,30–32], and it does not correlate well with the AE work presented in this paper.

While AE-based monitoring of metal-cutting processes is well studied [33], its use in bone cutting is rare. The two relevant pieces of literature include the bone drilling work of Liao et al. [19] and Guan et al. [20]. Liao et al. [19] demonstrated in-process detection of penetration depth during bone micro-drilling. A wavelet energy-based method was used to identify dominant frequencies in the AE signal at different penetration depths, which correlated to depth-related changes in bone properties. Similarly, Guan et al. [20] detected transitions between the cortical and cancellous regions of the bone for drilling procedures preceding the embedding of bone screws. However, in both these drilling studies, the AE sensor was again mounted on the bone sample as opposed to the tool, which is not practical for clinical translations. Furthermore, their work did not investigate fracture-cutting effects at the scale addressed in this paper.

There are two recent works in literature that have investigated *tool-mounted AE sensors* for bone cutting/scribing [21,34]. Mishra et al. [21] investigated the AE energy release rates encountered during shear-dominated conditions encountered in bone sawing. The continuous nature of AE signals reported in their work is different from the distinct fracture-related bursts seen in Fig. 4(*b*). Recently, Kataruka et al. [34] performed a microscopic assessment of bone toughness using scratch tests. In their work, a conical indenter instrumented with both a load-cell and AE sensor was used for scratch tests at varying penetration depths between 0.2–100 μm. This is one of the few studies where the overlay of indentation force is presented with an AE signature. While the AE signal in this scratching study is also a continuous signal, their work makes a case for the use of the AE signal to estimate fracture properties of bone.

Based on the survey of relevant literature presented earlier, it can be concluded that the findings of this paper related to the AE signatures obtained during fracture cutting of bovine cortical bone are unique. While the results appear promising, follow-on work must be performed under clinically relevant tooling and cutting conditions so as to mature these findings and to develop clinically translatable process-monitoring modalities. The use of data-enabled classification models similar to those used in process fault detection and correction in metal additive manufacturing [35] holds promise for this translation. Furthermore, studies like the one presented in this paper should be coupled with the approach taken by Kataruka et al. [34], where the AE data coupled with fundamental fracture mechanics theories is used to develop estimates of fracture toughness at the osteon-level. The recent follow-on work by Potukuchi et al. [25] demonstrates such a heuristic adaptation where the AE energy metrics associated with each of the dominant fractures cutting failure modes presented in this paper were used to estimate the cohesive zone parameters for a microstructure-based finite element model for facture cutting.

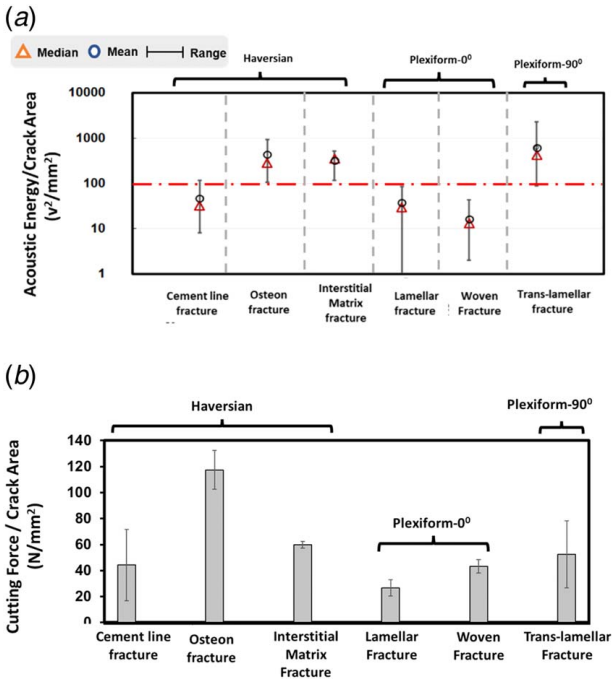

Fig. 8 Normalized acoustic energy and cutting force per unit crack area for specific failure mechanisms: (*a*) acoustic energy plotted on a log scale and (*b*) cutting force (Note: Horizontal line in (*a*) indicates clear demarcation levels between AE signals associated with each of the failure mechanisms)

4 Conclusions

This study investigated the acoustic emission signatures of dominant failure mechanisms encountered during fracture cutting of bovine cortical bone. The failure modes were identified through the synchronization of a high-speed camera with a tool-mounted cutting force and acoustic emission sensor. The following specific conclusions can be drawn from this work:

- The cutting force and acoustic emission signals provide complementary information regarding the failure process encountered during fracture cutting of bovine cortical bone. The acoustic emission signal is characterized by distinct transient bursts that correspond to specific fracture events. The cutting force signal is characterized by distinct peaks and valleys that have a direct correlation to specific AE bursts.
- All failure mechanisms except for interstitial matrix fracture (in haversian case) and woven fracture (plexiform—0 deg case) exhibit specific visually discernible patterns in the acoustic emission signatures. In the haversian case, osteon fracture resulted in the highest number of bursts as well as the maximum value of the amplitude ratios. For the plexiform case, the trans-lamellar fracture resulted in the maximum amplitude. In addition, the logarithmic normalized acoustic energies and the cutting force per unit crack area values are well correlated for each of the specific failure mechanisms. For the haversian bone, cement-line fracture and osteon fracture, respectively, consume the lowest and highest energy during fracture cutting. For the plexiform bone, the trans-lamellar fracture observed while cutting at 90 deg to the orientation of the lamella is seen to offer the most resistance to crack propagation.
- Overall, AE energies are clearly able to identify the lowest energy-consuming failure mode for the haversian case and the highest energy-consuming mode for the plexiform case. However, for the other cases, there is an overlap in the range of AE values even though statistical differences exist between the corresponding force magnitudes. The complementary nature of these signals has implications for tool-mounted sensing modalities that could be used to explore in-process failure mechanisms during bone surgical procedures.

Acknowledgment

The authors acknowledge funding support from the United States National Science Foundation CAREER award (CMMI 13-51275), as well as internal funding from Rensselaer Polytechnic Institute. Dr. Sri Krishna Sasidhar Potukuchi (Rensselaer PhD 2021) is acknowledged for his insightful discussions related to the experimental data sets.

Conflict of Interest

There are no conflicts of interest.

Data Availability Statement

The authors attest that all data for this study are included in the paper.

References

[1] Hofmann, S., Seitlinger, G., Djahani, O., and Pietsch, M., 2011, "The Painful Knee After TKA: A Diagnostic Algorithm for Failure Analysis," Knee Surgery, Sports Traumatol., Arthrosc.: Official J. ESSKA, **19**(9), pp. 1442–1452.
[2] Haenle, M., Skripitz, C., Mittelmeier, W., and Skripitz, R., 2012, "Economic Impact of Infected Total Knee Arthroplasty," Sci. World J., **2012**, pp. 1–6.
[3] Oduwole, K. O., Molony, D. C., Walls, R. J., Bashir, S. P., and Mulhall, K. J., 2010, "Increasing Financial Burden of Revision Total Knee Arthroplasty," Knee Surgery, Sports Traumatol., Arthrosc.: Official J. ESSKA, **18**(7), pp. 945–948.
[4] Patil, N., Lee, K., Huddleston, J. I., Harris, A. H., and Goodman, S. B., 2010, "Aseptic Versus Septic Revision Total Knee Arthroplasty: Patient Satisfaction, Outcome and Quality of Life Improvement," Knee, **17**(3), pp. 200–203.
[5] Dall, T. M., Gallo, P., Koenig, L., Gu, Q., and Ruiz, D., 2013, "Modeling the Indirect Economic Implications of Musculoskeletal Disorders and Treatment," Cost Effectiveness Resour. Allocation: C/E, **11**(1), p. 5.
[6] Jacobs, C. H., Pope, M. H., Berry, J. T., and Hoaglund, F., 1974, "A Study of the Bone Machining Process—Orthogonal Cutting," J. Biomech., **7**(2), pp. 131–136.
[7] Malak, S. F. F., and Anderson, I. A., 2008, "Orthogonal Cutting of Cancellous Bone With Application to the Harvesting of Bone Autograft," Med. Eng. Phys., **30**(6), pp. 717–724.
[8] Sugita, N., and Mitsuishi, M., 2009, "Specifications for Machining the Bovine Cortical Bone in Relation to Its Microstructure," J. Biomech., **42**(16), pp. 2826–2829.
[9] Liao, Z., and Axinte, D. A., 2016, "On Chip Formation Mechanism in Orthogonal Cutting of Bone," Int. J. Mach. Tools Manuf., **102**, pp. 41–55.
[10] Conward, M., and Samuel, J., 2021, "A Microstructure-Based Mechanistic Model for Bone Sawing: Part 1—Cutting Force Predictions," ASME J. Manuf. Sci. Eng., **143**(12), p. 121009.
[11] Conward, M., and Samuel, J., 2016, "Machining Characteristics of the Haversian and Plexiform Components of Bovine Cortical Bone," J. Mech. Behav. Biomed. Mater., **60**, pp. 525–534.
[12] Conward, M., and Samuel, J., 2023, "Microstructure-Based Failure Mechanisms Encountered During Fracture Cutting of Age-Varying Bovine Cortical Bone, 2023," ASME J. Manuf. Sci. Eng., **145**(6), p. 061004.
[13] Shu, L., and Sugita, N., 2020, "Analysis of Fracture, Force, and Temperature in Orthogonal Elliptical Vibration-Assisted Bone Cutting," J. Mech. Behav. Biomed. Mater., **103**, p. 103599.
[14] Sugita, N., Osa, T., Aoki, R., and Mitsuishi, M., 2009, "A New Cutting Method for Bone Based on Its Crack Propagation Characteristics," CIRP Ann., **58**(1), pp. 113–118.
[15] Sugita, N., Shu, L., Shimada, T., Oshima, M., Kizaki, T., and Mitsuishi, M., 2017, "Novel Surgical Machining via an Impact Cutting Method Based on Fracture Analysis With a Discontinuum Bone Model," CIRP Ann., **66**(1), pp. 65–68.
[16] Aggelis, D. G., Strantza, M., Louis, O., Boulpaep, F., Polyzos, D., and van Hemelrijck, D., 2015, "Fracture of Human Femur Tissue Monitored by Acoustic Emission Sensors," Sensors, **15**(3), pp. 5803–5819.
[17] Landis, E. N., and Baillon, L., 2002, "Experiments to Relate Acoustic Emission Energy to Fracture Energy of Concrete," ASCE J. Eng. Mech., **128**(6), pp. 698–702.
[18] Michlmayr, G., Cohen, D., and Or, D., 2011, "Sources and Characteristics of Acoustic Emissions From Mechanically Stressed Geologic Granular Media—A Review," Earth-Sci. Rev., **112**(3–4), pp. 97–114.
[19] Liao, Z., and Axinte, D. A., 2016, "On Monitoring Chip Formation, Penetration Depth and Cutting Malfunctions in Bone Micro-Drilling via Acoustic Emission," J. Mater. Process. Technol., **229**, pp. 82–93.
[20] Guan, F., Sun, Y., Qi, X., Hu, Y., Yu, G., and Zhang, J., 2018, "State Recognition of Bone Drilling Based on Acoustic Emission in Pedicle Screw Operation," Sensors, **18**(5), p. 1484.
[21] Mishra, R., Conward, M., and Samuel, J., 2021, "A Microstructure-Based Mechanistic Model for Bone Sawing: Part 2—Acoustic Energy Rate Predictions," ASME J. Manuf. Sci. Eng., **143**(12), p. 121010.
[22] Abdel-Wahab, A. A., Alam, K., and Silberschmidt, V. V., 2011, "Analysis of Anisotropic Viscoelastoplastic Properties of Cortical Bone Tissues," J. Mech. Behav. Biomed. Mater., **4**(5), pp. 807–820.
[23] Hoffseth, K., Randall, C., Chandrasekar, S., Hansma, P., and Yang, H. T. Y., 2017, "Analyzing the Effect of Hydration on the Wedge Indentation Fracture Behavior of Cortical Bone," J. Mech. Behav. Biomed. Mater., **69**, pp. 318–326.
[24] Carnelli, D., Lucchini, R., Ponzoni, M., Contro, R., and Vena, P., 2011, "Nanoindentation Testing and Finite Element Simulations of Cortical Bone Allowing for Anisotropic Elastic and Inelastic Mechanical Response," J. Biomech., **44**(10), pp. 1852–1858.
[25] Potukuchi, S. K. S., Conward, M., and Samuel, J., 2023, "Microstructure-Based Finite Element Model for Fracture Cutting of Bovine Cortical Bone," J. Manuf. Process, **101**, pp. 25–37.
[26] Krause, W. R., 1987, "Orthogonal Bone Cutting: Saw Design and Operating Characteristics," ASME J. Biomech. Eng., **109**(3), pp. 263–271.
[27] Wiggins, K. L., and Malkin, S., 1978, "Orthogonal Machining of Bone," ASME J. Biomech. Eng., **100**(3), pp. 122–130.
[28] Conward, M., 2018, Effects of Haversian and Plexiform Components on the Machining of Bovine Cortical Bone (Publication No. 13419372) Doctoral dissertation, Rensselaer Polytechnic Institute. ProQuest Dissertations and Theses database.
[29] Calzada, K. A., Kapoor, S. G., DeVor, R. E., Samuel, J., and Srivastava, A. K., 2012, "Modeling and Interpretation of Fiber Orientation-Based Failure Mechanisms in Machining of Carbon Fiber-Reinforced Polymer Composites," J. Manuf. Process., **14**(2), pp. 141–149.
[30] Kapur, R. A., 2016, "Acoustic Emission in Orthopaedics: A State of the Art Review," J. Biomech., **49**(16), pp. 4065–4072.
[31] Shridharani, J. K., Ortiz-Paparoni, M. A., Eynde, J. O., and Bass, C. R., 2021, "Acoustic Emissions in Vertebral Cortical Shell Failure," J. Biomech., **117**, p. 110227.
[32] Shrivastava, S., and Prakash, R., 2009, "Assessment of Bone Condition by Acoustic Emission Technique: A Review," J. Biomed. Sci. Eng., **2**(3), pp. 144–154.
[33] Kishawy, H. A., Hegab, H., Umer, U., and Mohany, A., 2018, "Application of Acoustic Emissions in Machining Processes: Analysis and Critical Review," Int. J. Adv. Manuf. Technol., **98**(5–8), pp. 1391–1407.
[34] Kataruka, A., Mendu, K., Okeoghene, O., Puthuvelil, J., and Akono, A.-T., 2017, "Microscopic Assessment of Bone Toughness Using Scratch Tests," Bone Rep., **6**, pp. 17–25.
[35] Ladani, L. J., 2021, "Applications of Artificial Intelligence and Machine Learning in Metal Additive Manufacturing (2021)," J. Phys.: Mater., **4**(4), p. 042009.